

Materials and process development for manufacturing porcelain figures using a binder jetting 3D printer

Jung Hoon Choi^{a,b}, Eun Tae Kang^b, Jin Wook Lee^a, Ung Soo Kim^{a,*} and Woo Seok Cho^a

^aKorea Institute of Ceramic Engineering & Technology, 3321 Gyeongchung-daero, Sindun-myeon, Icheon 17303, Korea

^bDivision of Materials Science & Engineering, Gyeongsang National University, 501 Jinju-daero, Jinju 52828, Korea

Raw materials and processes were developed to manufacture a porcelain figure using a binder jetting 3D printer. A digital sketch was created by considering the structural stability, and the optimal geometry and thickness (< 20 mm) were determined through thermal flow analysis. Dry glass beads, clay, and quartz were mixed in 34%, 46%, and 20% proportions, respectively. Alumina cement (5%) and sodium silicate powder (4%) were added to facilitate the curing process. The optimal particle size of the glass beads was found to be 86 μm from measurements of the angle of repose, and the flowability was further enhanced by adding 3% hydrophilic fumed silicas, whose specific surface area was 90 m²/g. Although the addition of hydrophobic fumed silicas caused a significant change in flowability, this material was not used in the experiment because of its incompatibility with the aqueous binder. Using bar-type sample sintering and glaze applicability measurements, we determined the optimal conditions for the glazing and heat treatment processes: the first sintering step was conducted at 1100 °C, followed by the second sintering at 1200 °C by applying a glaze with 50% solid content. The geometry match between the final porcelain figure and the digital sketch was up to 67% accurate when the surface texture was included, and up to 92% when only the skeletons were compared.

Key words: Raw materials, Porcelain, Binder Jetting, Flowability, Contact angle.

Introduction

Decorative porcelain figures of aesthetic value for interior and exterior design are produced in small quantities to meet the needs of diverse consumers and are sold at high prices. From this perspective, porcelain figures, among traditional ceramic products, are suitable for production by 3D printing technologies. In the case of existing porcelain figures, designers sketch the figure shapes and fabricate prototypes through extensive manual work based on the sketches. Gypsum molds are then manufactured using the completed prototypes, and the figures are fabricated through a slip casting process. After the figures are dried and the first sintering has been carried out, a glaze is applied and the second sintering is performed to produce the final products [1]. 3D printing technology makes it possible to avoid the manual fabrication of prototypes and gypsum molds in this porcelain figure manufacturing process, so that the desired objects are directly formed.

In the binder jetting 3D printing process, a powder is deposited to form a thin layer, and a binder solution is repeatedly sprayed on the layer and cured, to produce the final product [2-3]. The composition of the powder

has to be selected according to the nature of the product to be fabricated, and the characteristics of the powder, such as flowability, packing density, and pore size, must be chosen according to the characteristics of the binder jetting process [4]. In addition, the compatibility between the powder and the binder, along with the wettability and penetration time of the binder in the powder bed, must be taken into consideration [5-7].

To fabricate a porcelain figure composed of glass phases, quartz, and mullite after sintering, the starting materials (clay, feldspar, and quartz) must be combined in appropriate proportions [8]. The powder shape and size directly affect the flowability, packing density, and pore size [9-11]. Therefore, the shapes and the physical properties of the powders used, as well as their compositions, need to be optimized. The binder solution must permeate the powder bed in a fast and uniform way, and form links with the powders. After drying, it must maintain enough green strength to sustain the following step of the production process. For this purpose, auxiliary materials that can accelerate curing by reacting with the binder solution and increase the green strength are sometimes added to the material [12].

In this study, a material that can be used in binder jetting 3D printers was developed by supplementing existing clay-feldspar-quartz ceramic materials, and a porcelain figure was created using this material and sintered to produce the final product. The process

*Corresponding author:
Tel : +82-31-645-1422
Fax: + 82-31-645-1485
E-mail: ukim@kicet.re.kr

consists of three steps, i.e., digital sketching, optimization of the powder bed materials, and forming and sintering of the porcelain figure. We describe the details of each step and discuss the methods used to compare our process with existing ceramic manufacturing procedures.

Experiments

To fabricate a porcelain figure reproducing the “Moses” sculptured by Michelangelo, a digital sketch was created, taking into account the shrinkage and deformation occurring during the forming and sintering processes, and the consequent structural stability. To improve the surface texture of the figure, the curved portions of the hair and cloth were created using normal mapping, and design patterns were extracted. The optimal geometry and thickness were determined by conducting a thermal flow analysis of the completed digital sketch structure. The Delcam’s ArtCAM software was used to extract and process the design patterns, and the sculpting software was used to assemble and place them. Dassault’s SOLIDWORKS was used for the thermal distribution simulation of the final digital sketch.

Glass beads (mean particle size = 13 μm , Sovitec, France), quartz (Buyeo Quartz, BMS, Korea), and clay (EPK Clay, Edgar Minerals, USA) were used to produce the starting material. All glass beads used in the experiment were composed of soda lime silicate glass with a softening point of 730 $^{\circ}\text{C}$. Dry glass beads, clay, and quartz were mixed in 34, 46, and 20% proportions, respectively, in accordance with quantitative phase analysis results for existing ceramics after heat treatment. 5% alumina cement (UAC80N, Union, Korea) and 4% sodium silicate powder (Daejung, Korea) were added to facilitate the curing process.

To increase the flowability of the mixture, we studied the dependence of the angle of repose on the particle size of the spherical glass beads. While the other component materials were left unchanged, glass beads (Sovitec, France) with five different average particle sizes (13, 62, 86, 115, and 122 μm) were added, to compare the angle of repose and tap density. 0.5, 1.5, and 3.0% fumed silicas were added to the mixture giving the best results, and the angle of repose was measured. The fumed silicas used in the experiment were hydrophilic fumed silica FA & FB (FA: Konasil K-90, OCI, Korea & FB: Aerosil-200, Evonik, Germany) and hydrophobic fumed silica FC & FD (FC: Aerosil R-805 & FD: Aerosil R-972, Evonik, Germany). Their specific surface areas were 90, 200, 150, and 110 m^2/g , respectively.

The final composition was determined from these measurements, after which an experiment on the compatibility with the aqueous binder was conducted. The aqueous binder used in the experiment was a 5% PVA solution (HS-BD25, San Nopco Korea, Korea)

with 0.5% octamethylcyclotetrasiloxane (BYK 380, BYK, Germany) as a surface tension modifier. Powder beds were fabricated using the mixture with the final composition, and, once the aqueous binder was dropped, the initial contact angle and the bed penetration time were measured using a contact angle analyzer (Phoenix 400, SEO, Korea).

Bar-type samples were printed using the final composition and completely dried for the sintering experiment. The printer used in the experiment was a binder jetting Projet 360 (3D Systems, USA). The default binder jetting flow of the Projet 360 printer is 0.281 ml/cm^3 , which is not suitable for curing the powder that we developed. Changes in the green strength according to the spray amount were analyzed to determine the optimal binder jetting flow, which was found to be 0.507 ml/cm^3 . The dimensions of the printed samples were 10 (width) \times 100 (length) \times 5 mm^3 (thickness). After drying, the temperature was increased by 3 $^{\circ}\text{C}$ per min. The samples were maintained at the maximum temperature for 1 hr and then cooled. Maximum temperatures of 1000, 1100, 1200, and 1300 $^{\circ}\text{C}$ were considered to determine the density and water absorption dependence on the temperature (ASTM C373-14). The fracture surfaces of the samples were observed using a scanning electron microscope (SEM, JSM-6701F, JEOL, Japan).

Samples with dimensions of 40 (width) \times 120 (length) \times 7 mm^3 (thickness) were printed to examine the glaze applicability. After a glaze was applied to the samples sintered at 1100 $^{\circ}\text{C}$, the samples were again sintered at 1200 $^{\circ}\text{C}$, and the state of the glaze surface was examined. After the first sintering, two glaze types with different concentrations were applied twice, exploiting the high water absorption of the samples (glaze composition: feldspar 49%, limestone 17%, kaolin 6.3%, and quartz 27.7%). A dilute glaze (solid content 50%) was applied twice to one sample, and a dilute glaze and then a dense glaze (solid content 65%) were applied to a second sample. After glazing, both samples were sintered again at 1200 $^{\circ}\text{C}$.

The porcelain figure was formed through the 3D printing process using the final composition of the powder bed derived from the above experiment and the aqueous binder. The aqueous binder was sprayed at 0.507 ml/cm^3 . The shell area was sprayed with a 137% excess amount of material compared to the core area, to improve the surface strength. After the porcelain figure was completely dried and the first sintering was performed at 1100 $^{\circ}\text{C}$, a glaze was applied. Sintering was again performed at 1200 $^{\circ}\text{C}$, to give the final product. The digital information of the figure was extracted using a 3D scanner and compared with the digital sketch to assess quantitatively the accuracy of the completed figure. A Microscribe’s G2X system was used as 3D scanner, and Delcam’s PowerShape software was used for the match analysis.

Results and Discussion

Fig. 1(a) shows the digital sketch of the “Moses” sculpture made for this experiment. The thermal distribution analysis carried out using SOLIDWORKS Flow Simulation on the interior of the porcelain figure generated during the sintering process indicates that a temperature dispersion of up to 29.81 °C occurred in the area where the thickness was 20 mm or higher, which led to the appearance of cracks. Fig. 1(b) shows the temperature distribution in the cross section of the porcelain figure when the external temperature was set

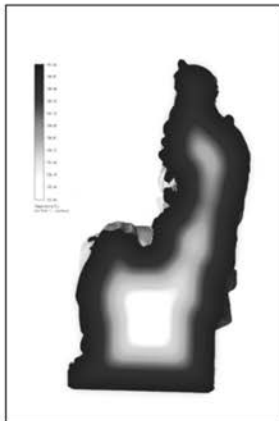


Fig. 1. (a) Digital sketch of “Moses” sculptured by Michelangelo, (b) thermal dispersion analysis of the porcelain figure when the external temperature was set to 770 °C, and (c) cross section of the porcelain figure being printed in the optimized structure.

to 770 °C. When the solid thickness of the digital sketch was changed to 20 mm or less to address this problem, the sintering process did not produce cracks. Fig. 1(c) shows the internal cross section of the porcelain figure being printed in these optimized conditions.

In ceramic manufacturing, objects are fabricated using a plastic body mixed with the starting materials, such as clay, feldspar, and quartz, which are treated at high temperature to form a glassy phase and crystalline phases, such as mullite and quartz [8]. It is known from previous studies that glassy phases, mullite, and quartz formed after sintering have relative ratios of 50-60%, 15-20%, and 20-30%, respectively. [13, 14]. In 3D printing, it is however necessary to reduce the sintering temperature of the ceramics. For this purpose, we developed a starting material in which feldspar was replaced by glass. Glass powder was used to reduce the heat consumed by the feldspar and quartz in standard materials to form glass phases through vitrification. Clay is an important component of the mixture, which maintains the forming strength and forms mullite at around 1200 °C during the heat treatment process. Quartz plays the role of a skeleton, and minimizes shrinkage and deformation during the forming and sintering processes.

The binder jetting 3D printing process involves the deposition of the powder, which is then cured using a liquid binder. Therefore, the flowability of the mixed materials is an important factor for the success of the process. The packing density also affects the green and sintering density of the product. To increase the flowability of the basic material that we developed, we studied the dependence of the angle of repose on the particle size of the spherical glass beads. Fig. 2 shows that the angle of repose decreases and then increases again with increasing glass bead particle size. In other words, the flowability increases with the particle size, but it decreases when the particle size exceeds a certain value. The optimal particle size of the glass beads was

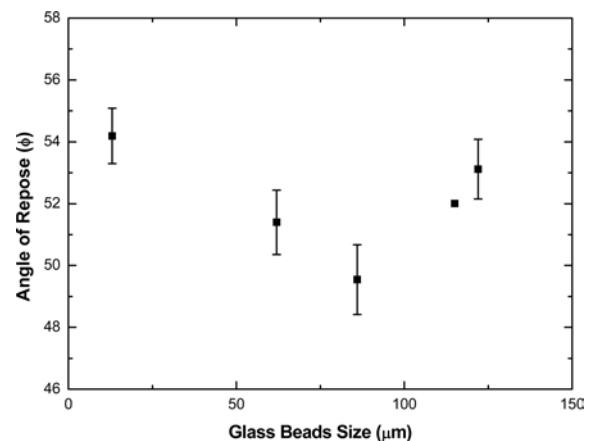


Fig. 2. Variation of the angle of repose with the mean particle size of the glass beads.

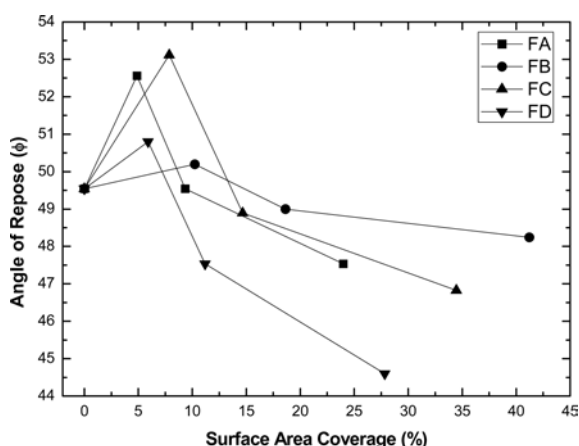


Fig. 3. Dependence of the angle of repose on the surface area coverage of fumed silicas over host powders.

found to be 86 μm , although glass beads in the range 86–100 μm were all found to give satisfactory results. When 13 μm glass beads were added, the tap density was 1.25 g/ml, whereas the tap density of the remaining samples was 1.30 g/ml. Considering the standard deviation in the density for all samples, these two values were considered similar in this work.

An angle of repose of 40–50° corresponds to a Carr's index indicating "low" to "poor" flowability. Nevertheless, it has been reported that repose angles in this range were successfully used in the manufacturing process in numerous cases. It has been argued, however, that angles of repose exceeding 50° are unsuitable [15]. In our case, the highest flowability was obtained when 86 μm glass beads were used, with an angle of repose of 49.5°. It is therefore necessary to reduce the angle of repose of the powder in order to obtain a stable binder jetting process.

0.5, 1.5, and 3.0% hydrophilic and hydrophobic fumed silicas were added to the powder containing the 86 μm glass beads, and the angle of repose was again measured. Fig. 3 shows that both the fumed silica surface characteristics and its specific surface area (particle size) affect the flowability of the powder. When the amount of added fumed silicas was converted to the surface coverage of the entire powder, the angle of repose for all samples was found to increase if the area covered was 10% or less, and to decrease again if the coverage exceeded 10%. When 0.5% fumed silicas were added, 10% or less of the surface of the host particles was unevenly coated, and the cohesive force of the powder was affected. It appears that an increase in the friction between the powder particles is responsible for the observed decrease in flowability. Overall, we found that a surface area coverage of 15% or more increases the flowability.

In the case of hydrophilic fumed silica addition, flowability was found to increase, but only by a limited

amount. Larger flowability was in general observed when hydrophobic fumed silicas were added, and we found that the hydrophobic fumed silica FD, with a 110 m^2/g specific surface area, was the most effective. At variance with hydrophobic fumed silicas, hydrophilic fumed silicas affect the flowability depending on the moisture content of the atmosphere. For hydrophilic fumed silica addition, the interparticle cohesion increases with the amount of atmospheric moisture, resulting in reduced flowability enhancement compared to hydrophobic fumed silicas [16, 17].

For identical fumed silica surface characteristics, flowability was found to be higher when the specific surface area of the particles was small. It is known that the smaller particle size of fumed silicas (high specific surface area) leads to better flowability [18, 19]. In this study, however, the opposite was observed. Although the reason of this trend is unknown, our results indicate that the guest particle size in a system where particles of various shapes and sizes are mixed is not the only factor affecting the flowability.

When the raw materials mixed with hydrophobic fumed silicas are used, it can be difficult for the aqueous binder solution to permeate the powder bed. To study this effect, we carried out permeation tests on three kinds of powder beds using the powders without fumed silicas, with hydrophilic fumed silicas (Konasil K-90), and with hydrophobic fumed silicas (Aerosil R-972). Each powder bed was prepared in a 7 ml petri dish, and the penetration of the dropped PVA aqueous binder into each bed was analyzed using a contact angle analyzer.

As shown in Fig. 4 and Table 1, it took 13.2 s on average for the aqueous binder to be fully absorbed in the bed when fumed silicas were not added, and only 6.8 s when hydrophilic fumed silicas were added. When hydrophobic fumed silicas were added, the binder was not absorbed and maintained the initial state even after 10 min. When powders are coated with hydrophilic or hydrophobic fumed silicas, the powders exhibit the same surface characteristics as those of the coating materials [20, 21]. Numerous hydroxyl groups are present on the surface of the hydrophilic fumed silica particles. Therefore, when the particles enter into contact with water, the spreading speed of the water through the pores of the powder increases, and the penetration time of the binder is reduced. Hydrophobic

Table 1. Contact angle and penetration time of an aqueous PVA binder in the powder beds prepared with or without fumed silicas.

	Contact angle (°)	Penetration time (s)
Powder bed	74.4 ± 7.2	13.2 ± 2.7
Powder bed with 3% FA	60.9 ± 1.9	6.8 ± 1.4
Powder bed with 3% FD	107.9 ± 5.9	NA

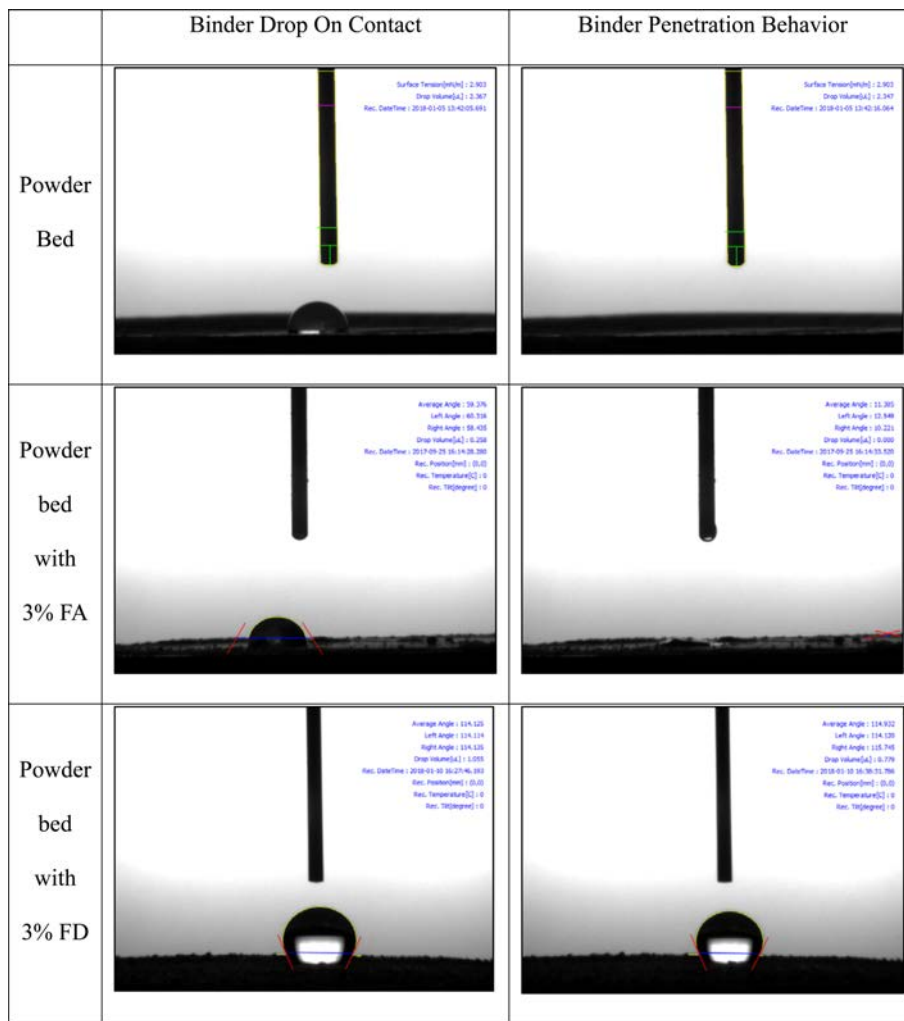


Fig. 4. Penetration behavior of an aqueous PVA binder in powder beds prepared with or without fumed silicas.

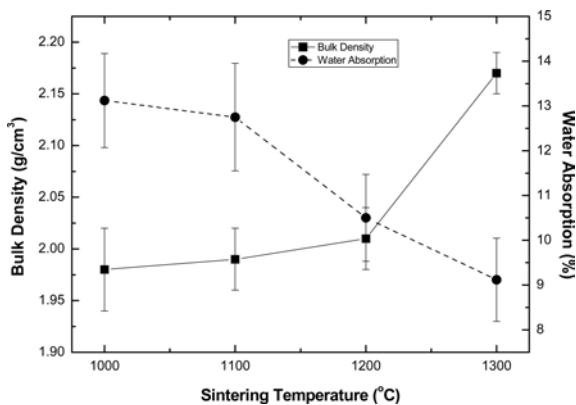


Fig. 5. Bulk density and water absorption of bar samples sintered at 1000, 1100, 1200, and 1300 °C.

fumed silicas have the opposite effect.

The compatibility between the powder bed with fumed silicas of different characteristics and the aqueous binder can also be assessed by considering the initial contact angle (Table 1). The contact angle between the powder bed and the aqueous binder was 74.4 ° when fumed silicas were not added, 60.9 ° when

hydrophilic fumed silicas were added, and 107.9 ° when hydrophobic fumed silicas were added. Based on these results, powders with 3.0% hydrophilic FA fumed silica added were chosen as final materials, because of their compatibility with the aqueous binder, even though their flowability was lower than that of the samples containing hydrophobic fumed silicas.

Bar-type samples were printed using the final mixture, dried completely, and subjected to a sintering experiment (Fig. 5). When the sintering temperature was increased from 1000 to 1300 °C, the density was found to increase from 1.98 to 2.17 g/cm³ and the water absorption to decrease from 13.12 to 9.12%. The sintering density was found to be lower and the water absorption higher compared to samples fabricated using typical ceramic manufacturing processes, owing to the initial particle size of the starting materials and to the low shear force of the 3D printing process. When sintering was performed at 1000 °C or higher, however, a sufficient strength was achieved to sustain the following processing step. We confirmed through the observation of the microstructure of the fracture surface that liquid phases between particles were dense

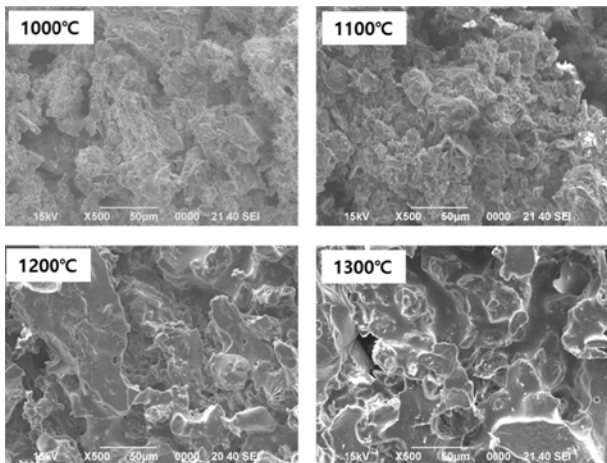


Fig. 6. SEM image on the fractured surface of bar samples heated at 1000, 1100, 1200, and 1300 °C.

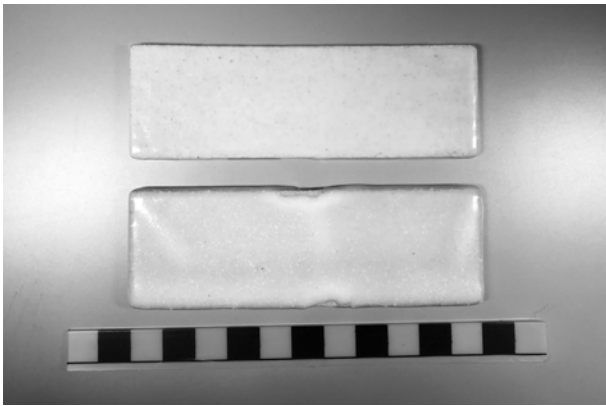


Fig. 7. Bar sample double glazed with a dilute glaze suspension (above) and bar sample glazed with a dilute glaze and a dense glaze in sequence (below) after the sintering process.

and uniformly distributed for the samples sintered at 1200 °C or higher (Fig. 6).

To test the applicability of the existing glazing process to samples characterized by high water absorption, the condition of the glaze surface was examined after sintering at 1100 °C and again at 1200 °C. As shown in Fig. 7, the doubly glazed sample with a dilute glaze maintained transparency while a uniform glaze layer was being formed. In the case of the sample glazed with a dilute glaze followed by a dense glaze, the glaze layer formed was found to be too thick. Based on these results, double-glazing with a dilute glaze was selected as the optimal glazing process.

The ceramic figure was created using 3D printing with a powder bed with the composition derived above and the aqueous binder. As shown in Fig. 8(a), the ceramic figure was successfully fabricated. The final product was less than 17 cm in size after sintering and maintained the complicated shape of the original design. The geometry match between the completed figure and the digital sketch was up to 67% accurate when the surface texture was considered, and up to

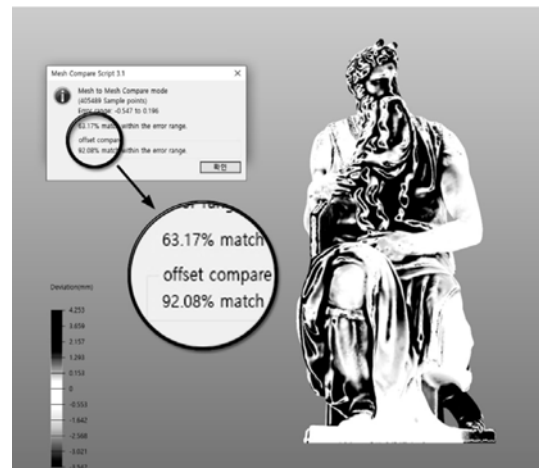


Fig. 8. (a) Image of the final porcelain figure, and (b) analysis of the consistency of the final porcelain figure with the digital sketch.

92% when only the skeletons were compared (Fig. 8(b)). The lower accuracy determined by the inclusion of the surface texture in the comparison appears to be caused by the surface coating effect of the glaze.

Conclusions

Raw materials and processes were developed to manufacture porcelain figures using a binder jetting 3D printer. A digital sketch was created taking into account the structural stability during shrinkage and deformation, which can occur during the forming and sintering processes. The optimal geometry and thickness (< 20 mm) were determined through thermal flow analysis.

Dry glass beads, clay, and quartz were mixed in 34, 46, and 20% proportions, respectively. Alumina cement (5%) and sodium silicate powder (4%) were added, to facilitate the curing process. The optimal particle size of the spherical glass beads for flowability was determined to be 86 µm by monitoring the dependence

of the angle of repose on the particle size.

Hydrophilic and hydrophobic fumed silicas were added to increase flowability, and we found that a surface area coverage of 15% or higher determines a measurable increase in flowability. Hydrophilic fumed silicas showed only limited effects on the flowability, while hydrophobic fumed silicas clearly enhanced the flowability. When the surface characteristics of the fumed silicas were identical, the flowability was found to increase more for particles of small surface area.

A compatibility experiment was conducted to measure the penetration time and the contact angle of the aqueous binder in the powder beds. It took 13.2 s on average for the aqueous binder to be fully absorbed in the bed in the absence of fumed silicas, but only 6.8 s when hydrophilic fumed silicas were added. When hydrophobic fumed silicas were added, the binder was not absorbed and maintained the initial state even after 10 min.

The contact angle between the powder bed and the aqueous binder was 74.4° in the absence of fumed silicas, 60.9° when hydrophilic fumed silicas were added, and 107.9° when hydrophobic fumed silicas were added. Based on these results, powders with 3.0% hydrophilic fumed silica FA added were chosen as the final material, because of their compatibility with the aqueous binder, even though their flowability was lower than that measured in the presence of hydrophobic fumed silicas.

Bar-type sample sintering experiments and glaze applicability experiments were used to determine the optimal conditions for the glazing and heat treatment processes. We found that first sintering at 1100 °C, followed by second sintering at 1200 °C with the application of a glaze with a 50% solid content, was the most suitable procedure.

The geometry match between the porcelain figure obtained using the final powder composition and the development process described above and the digital sketch was up to 67% accurate when the surface texture was included in the comparison and up to 92% accurate when only the skeletons were considered.

Acknowledgements

This work was supported by the Technology Innovation Program (10070165, Convergence of Traditional Ceramicware Process and Digital 3D Printing Process for

High Value Added Bone China Porcelain) funded by the Ministry of trade, Industry & Energy (MOTIE, Korea).

References

1. J. Simó, R. Vivó, A. Crespo, and J. F. Blanes, M. Martinez, IFAC Proceedings 31[31] (1998) 127-132.
2. E. Sachs, M. Cima, P. Williams, D. Brancazio, and J.
3. Cornie, J. Eng. Ind. 114[4] (1992) 481-488.
4. J. Deckers, J. Vleugels, J.-P. Kruth, J. Ceram. Sci. Tech. 05[04] (2014) 245-260.
5. A. Cooke and J. Slotwinski, in "Properties of Metal Powders for Additive Manufacturing: A review of the State of the Art of Metal Powder Property Testing" (National Institute of Standards and Technology, 2012) p. 5,6,10-19.
6. H. Miyajiri and L. Yang, in Proceedings of the 27th international solid Freeform Fabrication Symposium, August 2016 (University of Texas at Austin, 2016), edited by D. L. Bourell, R. H. Crawford, C. C. Seepersad, J. J. Beaman, S. Fish, and H. Marcus, p. 1945-1959.
7. B. M. Wu and M. J. Cima, Polym. Eng. Sci. 3[2] (1999) 249-260.
8. Moon, J. E. Grau, V. Knezvic, M. J. Cima, and E. M. Sachs, J. Am. Ceram. Soc. 85[4] (2002) 755-762. W. M. Carty and U. Senapati, J. Am. Ceram. Soc. 81[1] (1998) 3-20.
9. J. S. Reed, in "Principles of Ceramics Processing" (John Wiley & Sons, Inc., 1995) p. 215-230.
10. H. Masuda, K. Higashitani, and H. Yoshida, in "Powder Technology Handbook" (CRC Press, 2006) p. 350-359.
11. G. Lumay, F. Boschini, K. Traina, S. Bontempi, J. -C. Remy, R. Cloots, and N. Vandewalle, Powder Technol. 224 (2012) 19-27.
12. G. Marchelli, M. Ganter, and D. Storti, in Proceedings of the 20th international solid Freeform Fabrication Symposium, August 2009 (University of Texas at Austin, 2009), edited by D. L. Bourell, R. H. Crawford, C. C. Seepersad, J. J. Beaman, S. Fish, and H. Marcus, p. 477-487.
13. J. Kim, E. Heo, S. Kim, and J. Kim, J. Korean Phys. Soc. 68[1] (2016) 126-130.
14. J. Martin-Marquez, A. G. De la Torre, M. A. G. Aranda, J. Ma Rincón, and M. Romero, J. Am. Ceram. Soc. 92[1] (2009) 229-234.
15. U. S. Pharmacopeial Convention in "Pharmacopeia USP35-NF 30" (USP, 2012) p. 801-802
16. V. Karde, and C. Choro, Int. J. Pharm. 485 (2015) 192-201.
17. L. Qu, Q. Zhou, J. a. Denman, P. J. Stewart, K. P. Hapgood, and D. A. V. Morton, Eur. J. Pharm. Sci. 78 (2015) 264-272.
18. T. Kojima and J. A. Elliott, Chem. Eng. Sci. 101 (2013) 325-328.
19. J. Yang, A. Silva, A. Banerjee, R. N. Dave, and R. Pfeffer, Powder Technol. 158 (2005) 21-33.
20. V. Karde and C. Ghoroi, Int. J. Pharm. 475 (2014) 351-363.
21. G. Lefebvre, L. Galet, and A. Chamayou, AIChE J. 57[1] (2011) 79-86.